optica

Hard x-ray multi-projection imaging for single-shot approaches

P. Villanueva-Perez,[1,2,*] ☉   B. Pedrini,[1]   R. Mokso,[1,3]   P. Vagovic,[2]   V. A. Guzenko,[1] ☉   S. J. Leake,[4] ☉
P. R. Willmott,[1]   P. Oberta,[5]   C. David,[1]   H. N. Chapman,[2,6,7] ☉   AND   M. Stampanoni[1,8]

[1]*Paul Scherrer Institut, 5232 Villigen PSI, Switzerland*
[2]*Center for Free-Electron Laser Science (CFEL), DESY, Notkestrasse 85, 22607 Hamburg, Germany*
[3]*Max IV Laboratory, Lund University, SE-221 00 Lund, Sweden*
[4]*ESRF, The European Synchrotron, 71 Avenue des Martyrs, 38000 Grenoble, France*
[5]*Institute of Physics, Academy of Sciences of the Czech Republic v.v.i., 18221 Prague, Czech Republic*
[6]*Department of Physics, University of Hamburg, Luruper Chaussee 149, 22761 Hamburg, Germany*
[7]*Centre for Ultrafast Imaging, Luruper Chaussee 149, 22761 Hamburg, Germany*
[8]*Institute for Biomedical Engineering, UZH/ETH Zürich, 8093 Zürich, Switzerland*
Corresponding author: pablo.villanueva-perez@cfel.de

High-brilliance x-ray sources (x-ray free-electron lasers or diffraction-limited storage rings) allow the visualization of ultrafast processes in a 2D manner using single exposures. Current 3D approaches scan the sample using multiple exposures, and hence they are not compatible with single-shot acquisitions. Here we propose and verify experimentally an x-ray multi-projection imaging approach, which uses a crystal to simultaneously acquire nine angularly resolved projections with a single x-ray exposure. When implemented at high-brilliance sources, this approach can provide volumetric information of natural processes and non-reproducible samples in the micrometer to nanometer resolution range, and resolve timescales from microseconds down to femtoseconds. © 2018 Optical Society of America under the terms of the [OSA Open Access Publishing Agreement](#)

https://doi.org/10.1364/OPTICA.5.001521

Since their discovery, hard x rays have been crucial in the natural sciences because of their penetration power and short wavelength, which allows high-resolution imaging of thick samples, even in native conditions. Among the currently used x-ray imaging techniques, phase-contrast methods enhance the contrast sensitivity by exploiting the phase shift due to variations in the electron density, rather than the intensity attenuation characteristic of radiographic approaches [1]. Coherent techniques, which exploit phase contrast, are regarded as the most suitable to achieve high resolution [2], in that they can address micrometer to nanometer scales. Because the high brilliance is the key parameter for coherent techniques, their advent coincided with the realization of third-generation synchrotron light sources. Novel x-ray sources with orders of magnitude higher brilliance, such as diffraction-limited storage rings [3] and x-ray free-electron lasers (XFELs) [4–6], enlarge the spectrum of coherent applications, especially

addressing shorter timescales [7,8]. XFELs, in particular, provide ultra-intense femtosecond pulses, which can image samples before inducing any radiation damage [9]. This concept, known as diffract before destroy, was demonstrated experimentally [10] by reconstructing an object from an x-ray pulse, but before it Coulomb explodes. The resolution and contrast sensitivity are limited by the number of photons available in a single pulse, and not by the maximum tolerable dose that preserves a given resolution [11], as is the case for continuous sample illumination. As a consequence, any method that requires multiple exposures of the same sample, including three-dimensional (3D) techniques such as tomography [12,13] and confocal microscopy [14], or any scanning technique cannot be applied. Thus, XFEL applications aiming at 3D structural information, which deliver a high dose, either require imaging of several identical copies of the object [15] or are restricted to retrieving partial information from a single exposure [16], as desired in ankylography [17].

Here we propose a scheme christened x-ray multi-projection imaging (XMPI), which provides 3D structural information via multiple 2D projections at different tomographic angles acquired simultaneously from the same object. The key component of XMPI is a beam splitter that generates a number of beams by Laue diffraction, which illuminate a sample simultaneously from different angles. Each of these beams retains the corresponding projection information. This idea was proposed in 1994 for the soft x-ray regime [18] using a phase-grating splitter. In the hard x-ray regime under consideration, however, suitable gratings are unrealistic; for example, the grating pitch required to achieve a deflection for the first diffracted order of 20° for 4 keV photons would be 8.5 Å, which is too small for presently known manufacturing methods. In contrast, Laue diffracted beams are much more suitable because the deflection angles reach tens of degrees, making them compatible with the requirement for true tomographic projections. In a general case, the Laue condition can be achieved simultaneously for two different reflections by appropriately
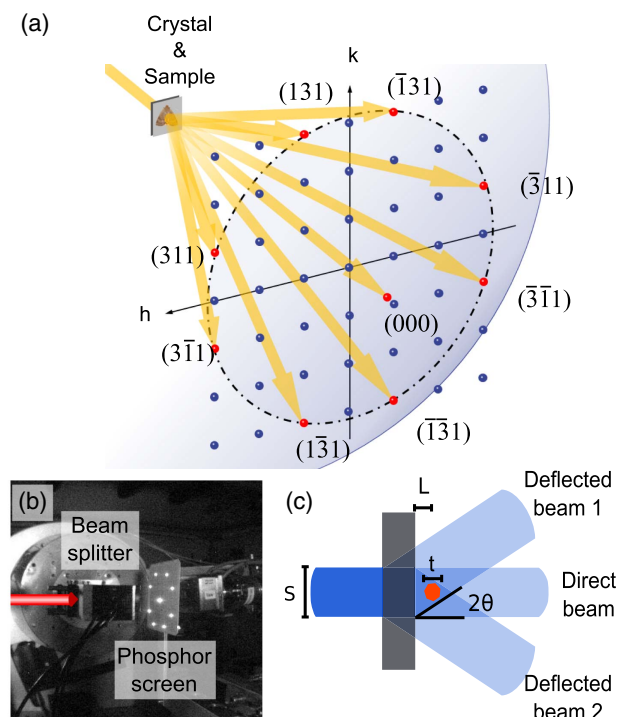
Fig. 1. Beam splitter. (a) Illustration of the eight reflections in reciprocal space of the {113}-family of a face-centered cubic crystal. The dotted-dashed curve represents the intersection between the Ewald sphere and the $l = 1$ plane. The sample is positioned downstream from the crystal to be illuminated by all the generated beams. (b) Image of the direct beam and of the eight diffracted beams on a phosphor screen, generated from a single incoming beam traversing a 100 μm thick Si(001) crystal perpendicular to the (001) surface. (c) Representation of the requirement of the maximum distance L from the crystal beam splitter surface to the sample such that the latter is illuminated by both the direct and the diffracted beams. The relevant parameters are the diameter of the direct beam S, the transverse extension of the sample t, and the deflection angle 2θ of the diffracted beam.

Fig. 2. Near-field imaging experiment. (a) Experimental setup used at the TOMCAT beamline of the Swiss Light Source. (b)–(d) Phase contrast images in the near-field regime recorded with the area detector placed in the horizontal plane at deflection angles of (b) 0° (direct beam direction), (c) 18.2° [diffracted beam from the Si(111) reflection], and (d) 35.1° [diffracted beam for the Si(311) reflection]. The detection plane was perpendicular to the direct beam. The rotation axes and rotation directions with respect to the projection in (a) are marked with dashed red lines and black arrows. The scale bar in (b) corresponds to 500 μm, and the two red dashed lines illustrate the angle between the rotation axes.

orienting the crystal [19]. This number can be increased by exploiting symmetries of the crystal lattice, setting the x-ray energy to specific values, and positioning the crystal so that several reflections sit simultaneously on the Ewald sphere. Figure 1(a) illustrates the generation of eight deflected beams by the {113}-family of Laue reflections of a face-centered cubic crystal, such as diamond or silicon. The incoming beam direction, defined by its momentum vector $\vec{k}_0$, is set parallel to a high-symmetry axis, corresponding to the (001)-reflection direction in the depicted example. All reflections related by a rotation around the symmetry axis, e.g., corresponding to {113}-family, form identical angles $\pi/2 - \theta$ with respect to the incoming beam direction and share the same reflection plane spacing d. The Laue condition for the wavelength λ,

$$\lambda = 2d \, \sin(\theta), \qquad (1)$$

is then fulfilled simultaneously by all eight planes, yielding eight diffracted beams with a deflection angle of 2θ. For a silicon crystal, the photon energy that sets the {113} planes in the Laue condition is 12.56 keV (see Supplement 1). Figure 1(b) provides experimental evidence for the simultaneous generation of the eight beams described above. The experiment was performed
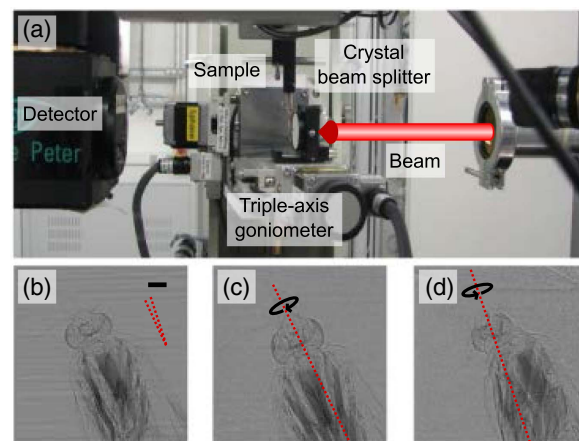
at the Materials Science beamline [20] of the Swiss Light Source (SLS), using a silicon crystal with the aforementioned arrangement. Figure 1(c) shows the arrangement of the beam splitter crystal and a sample positioned downstream the crystal in the overlap region of all eight diffracted beams. To ensure the simultaneous illumination of a sample of size t by all the beams, the incoming beam diameter S and maximum distance from the sample center to the closest face of the crystal L are constrained (see Supplement 1).

XMPI is a technique that can be applied to the near-field and far-field imaging regimes. In this work, we demonstrate that the different projections of an object are retrieved for both regimes with resolutions around 17 μm and 80 nm, respectively.

The near-field imaging experiment was carried out at the TOMCAT beamline at SLS [21]. Propagation-based phase-contrast imaging was performed (see Supplement 1) using the setup depicted in Fig. 2(a). The collimated beam at 12.56 keV illuminated a Si(001) splitter mounted on a triple-axis goniometer. Due to geometrical limitations of the experimental setup, the crystal could not be oriented to simultaneously hit the eight reflections of the Si {113}-family [Fig. 1(a)], but only the Si(131) and the Si(111) reflections, with deflections angles of 35.1° and 18.2°, respectively. A moth placed directly downstream from the splitter was illuminated simultaneously by the three beams. Three near-field images, shown in Figs. 2(b)–2(d), were recorded by translating the detector to intercept each of the three beams. The forward-direction image exhibits lower noise because of the higher intensity. The image resolution of such images was estimated to be about 17 μm based on analyzing the edge profiles. The rotation axes that relate the direct-beam projection [Fig. 2(b)] with the two deflected beam projections [Figs. 2(c) and 2(d)] form the expected angle of 11.9°. The features of the moth head observed in
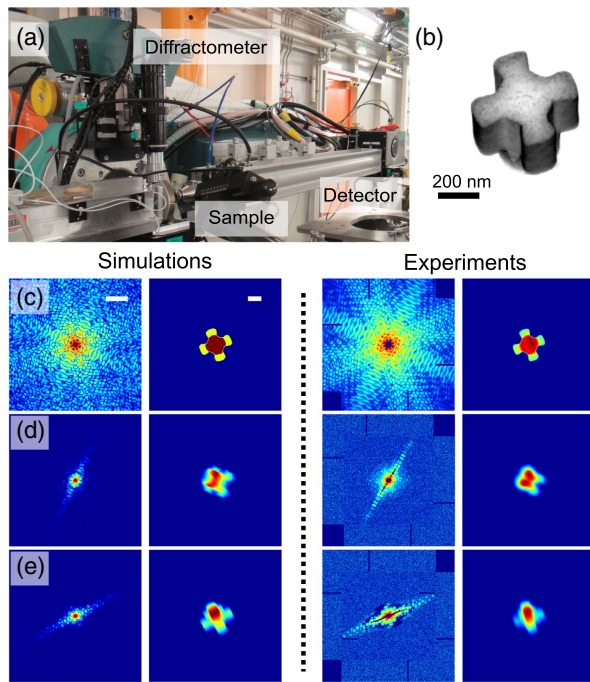
Fig. 3. Far-field imaging experiment. (a) Experimental setup used at the ID01 beamline of the ESRF synchrotron; (b) SEM image of the gold nanostructure sample; (c)–(e) data related to (c) the direct beam and (d), (e) the two accessible projections. From left to right, columns show the simulated diffraction pattern, corresponding simulated object projection, experimental diffraction pattern, and corresponding CDI reconstruction. The scale bars in the diffraction patterns and in the reconstructions correspond to 2×10^{-2} nm^{-1} and 200 nm, respectively.

Fig. 4. 3D reconstructions (see Visualization 1). These panels depict the retrieved object (yellow) compared to the simulated phantom (semi-transparent red) projected along (a) a direction perpendicular to the direct beam, (b) the direct beam, and (c) an arbitrary direction. The scale bar in (a) corresponds to 200 nm.

the three images concur with being projections of the same object along the directions given by (001), (111), and ($\overline{1}\,\overline{3}\,1$).

The far-field imaging experiment at 12.56 keV was performed at the ID01 beamline of the European Synchrotron Research Facility (ESRF) [22]. We performed coherent diffraction imaging (CDI) [23], a well-established technique at storage rings and XFELs [2], using the setup shown in Fig. 3(a). A Si(001) splitter was mounted on a small hexapod to adjust the orientation. The crystal was oriented such that the two {113}-family diffracted beams accessible in the ID01 diffractometer geometry were seen simultaneously on a pixel detector. A gold nanostructure exhibiting nontrivial 3D features [Fig. 3(b)] and grown on a silicon nitride membrane was glued on the downstream surface of the crystal. As the coherent flux was not sufficient, the beam was focused to a size of about $S = 1$ μm at the crystal surface with a numerical aperture, which matched the Darwin width of the Si (131) reflection [24,25]. Unfortunately, the beam diameter S was not sufficient to illuminate the sample simultaneously by all the generated beams. However, this is not a limitation at sources with higher coherent flux such as XFELs and diffraction-limited synchrotrons. The sample was then translated transversely to produce diffraction patterns on the detector positioned at a distance of 2.37 m. The three recorded diffraction patterns are shown in the third column of panels in Figs. 3(c)–3(e), along with corresponding simulations (first column) with the same signal levels. The experimental patterns from the diffracted beam clearly manifest larger background levels due to lower flux and background components enhanced by the crystal. The CDI reconstructions
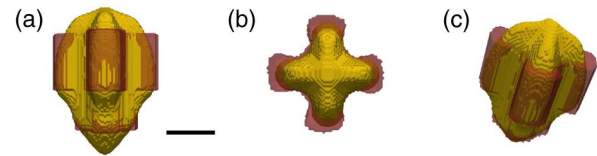
from the experimental diffraction images, obtained by applying phase retrieval algorithms, and the simulated projections of the sample are shown in the fourth and second columns, respectively, of the abovementioned panels. Their comparison confirms that the expected projections have been measured. The resolution of the reconstructions, established using the phase-retrieval transfer function criterion [26], was 18 nm for the direct beam projection and 77 and 85 nm for the two skew projections. A 3D reconstruction of the object using the three measured projections is depicted in Fig. 4. The reconstruction in yellow is compared to the simulated model in semi-transparent red. For further experimental and data analysis details, see Supplement 1.

In conclusion, we have experimentally validated XMPI, which relies on a single crystal as the beam splitter to simultaneously generate tomographic projections from a single exposure of a sample to the x rays. XMPI circumvents rotating the sample as for tomography and represents a clear improvement with respect to pseudo-3D single-shot methods. We conceived XMPI as an x-ray imaging method for XFELs. In the optical domain, similar concepts can be devised to retrieved 3D information with ultra-short laser pulses. In the diffract-before-destroy approach, which is essential to achieve submicrometer resolution from weakly scattering, nonreproducible objects, XMPI paves the way to 3D object reconstructions. Other applications, however, appear to be meaningful. If XFELs that offer pulse trains at megahertz repetition rates, such as the European XFEL or the Linac Coherent Light Source after the planned upgrade, are operated at fluences below the sample damage threshold, XMPI may enable to track the 3D structural dynamics of stochastic and deterministic [27] processes at the sub-microsecond timescale. At synchrotron facilities, XMPI may find applications in cases where a sample cannot be rotated due to the complexity of the sample environment. Furthermore, at diffraction-limited sources, such as at MAX IV Laboratory and future ones, the time resolution for structural dynamics investigations may be reduced well below the millisecond regime. We, therefore, anticipate that dedicated XMPI instruments may be realized at operational and future hard x-ray user facilities.

See Supplement 1 for supporting content.

REFERENCES

1. A. Sakdinawat and D. Attwood, Nat. Photonics **4**, 840 (2010).
2. H. N. Chapman and K. A. Nugent, Nat. Photonics **4**, 833 (2010).
3. M. Eriksson, J. F. van der Veen, and C. Quitmann, J. Synchrotron Radiat. **21**, 837 (2014).
4. P. Emma, R. Akre, J. Arthur, R. Bionta, C. Bostedt, J. Bozek, A. Brachmann, P. Bucksbaum, R. Coffee, F. J. Decker, Y. Ding, D. Dowell, S. Edstrom, A. Fisher, J. Frisch, S. Gilevich, J. Hastings, G. Hays, P. Hering, Z. Huang, R. Iverson, H. Loos, M. Messerschmidt, A. Miahnahri, S. Moeller, H. D. Nuhn, G. Pile, D. Ratner, J. Rzepiela, D. Schultz, T. Smith, P. Stefan, H. Tompkins, J. Turner, J. Welch, W. White, J. Wu, G. Yocky, and J. Galayda, Nat. Photonics **4**, 641 (2010).
5. T. Ishikawa, H. Aoyagi, T. Asaka, Y. Asano, N. Azumi, T. Bizen, H. Ego, K. Fukami, T. Fukui, Y. Furukawa, S. Goto, H. Hanaki, T. Hara, T. Hasegawa, T. Hatsui, A. Higashiya, T. Hirono, N. Hosoda, M. Ishii, T. Inagaki, Y. Inubushi, T. Itoga, Y. Joti, M. Kago, T. Kameshima, H. Kimura, Y. Kirihara, A. Kiyomichi, T. Kobayashi, C. Kondo, T. Kudo, H. Maesaka, X. M. Maréchal, T. Masuda, S. Matsubara, T. Matsumoto, T. Matsushita, S. Matsui, M. Nagasono, N. Nariyama, H. Ohashi, T. Ohata, T. Ohshima, S. Ono, Y. Otake, C. Saji, T. Sakurai, T. Sato, K. Sawada, T. Seike, K. Shirasawa, T. Sugimoto, S. Suzuki, S. Takahashi, H. Takebe, K. Takeshita, K. Tamasaku, H. Tanaka, R. Tanaka, T. Tanaka, T. Togashi, K. Togawa, A. Tokuhisa, H. Tomizawa, K. Tono, S. Wu, M. Yabashi, M. Yamaga, A. Yamashita, K. Yanagida, C. Zhang, T. Shintake, H. Kitamura, and N. Kumagai, Nat. Photonics **6**, 540 (2012).
6. C. Pellegrini, Phys. Scr. **T169**, 014004 (2016).
7. A. Barty, J. Phys. B **43**, 194014 (2010).
8. E. Weckert, IUCrJ **2**, 230 (2015).
9. R. Neutze, R. Wouts, D. van der Spoel, E. Weckert, and J. Hajdu, Nature **406**, 752 (2000).
10. H. N. Chapman, A. Barty, M. J. Bogan, S. Boutet, M. Frank, S. P. Hau-Riege, S. Marchesini, B. W. Woods, S. Bajt, W. H. Benner, R. A. London, E. Plönjes, M. Kuhlmann, R. Treusch, S. Düsterer, T. Tschentscher, J. R. Schneider, E. Spiller, T. Möller, C. Bostedt, M. Hoener, D. A. Shapiro, K. O. Hodgson, D. van der Spoel, F. Burmeister, M. Bergh, C. Caleman, G. Huldt, M. M. Seibert, F. R. N. C. Maia, R. W. Lee, A. Szöke, N. Timneanu, and J. Hajdu, Nat. Phys. **2**, 839 (2006).
11. M. R. Howells, T. Beetz, H. N. Chapman, C. Cui, J. M. Holton, C. J. Jacobsen, J. Kirz, E. Lima, S. Marchesini, H. Miao, D. Sayre, D. A. Shapiro, J. C. H. Spence, and D. Starodub, J. Electron Spectrosc. Relat. Phenom. **170**, 4 (2009).
12. A. M. Cormack, J. Appl. Phys. **35**, 2908 (1964).
13. G. N. Hounsfield, Br. J. Radiol. **46**, 1016 (1973).
14. P. Davidovits and M. D. Egger, Nature **223**, 831 (1969).
15. T. Ekeberg, M. Svenda, C. Abergel, F. R. N. C. Maia, V. Seltzer, J. M. Claverie, M. Hantke, O. Jönsson, C. Nettelblad, G. van der Schot, M. Liang, D. P. Deponte, A. Barty, M. M. Seibert, B. Iwan, I. Andersson, N. D. Loh, A. V. Martin, H. Chapman, C. Bostedt, J. D. Bozek, K. R. Ferguson, J. Krzywinski, S. W. Epp, D. Rolles, A. Rudenko, R. Hartmann, N. Kimmel, and J. Hajdu, Phys. Rev. Lett. **114**, 098102 (2015).
16. H. Wei, Nature **480**, E1 (2011).
17. K. S. Raines, S. Salha, R. L. Sandberg, H. Jiang, J. A. Rodríguez, B. P. Fahimian, H. C. Kapteyn, J. Du, and J. Miao, Nature **463**, 214 (2010).
18. M. R. Howells, C. J. Jacobsen, and S. Lindaas, "Possibility for one-shot tomography using a high-gain free-electron laser," Scientific Applications of Coherent X-Rays (1994), Report LBNL/ALS–652.
19. K. E. Schmidt, J. C. H. Spence, U. Weierstall, R. Kirian, X. Wang, D. Starodub, H. N. Chapman, M. R. Howells, and R. B. Doak, Phys. Rev. Lett. **101**, 115507 (2008).
20. P. R. Willmott, D. Meister, S. J. Leake, M. Lange, A. Bergamaschi, M. Böge, M. Calvi, C. Cancellieri, N. Casati, A. Cervellino, Q. Chen, C. David, U. Flechsig, F. Gozzo, B. Henrich, S. Jäggi-Spielmann, B. Jakob, I. Kalichava, P. Karvinen, A. Krempasky, A. Lüdeke, R. Lüscher, S. Maag, C. Quitmann, M. L. Reinle-Schmitt, T. Schmidt, B. Schmitt, A. Streun, I. Vartiainen, M. Vitins, X. Wang, and R. Wullschleger, J. Synchrotron Radiat. **20**, 667 (2013).
21. M. Stampanoni, A. Groso, A. Isenegger, G. Mikuljan, Q. Chen, A. Bertrand, S. Henein, R. Betemps, U. Frommherz, P. Böhler, D. Meister, M. Lange, and R. Abela, Proc. SPIE **6318**, 63180M (2006).
22. S. J. Leake, V. Favre-Nicolin, E. Zatterin, M. I. Richard, S. Fernandez, G. Chahine, T. Zhou, P. Boesecke, H. Djazouli, and T. U. Schülli, Mater. Des. **119**, 470 (2017).
23. J. Miao, P. Charalambous, J. Kirz, and D. Sayre, Nature **400**, 342 (1999).
24. C. G. Darwin, Philos. Mag. **27**(158), 315 (1914).
25. C. G. Darwin, Philos. Mag. **27**(160), 675 (1914).
26. D. Shapiro, P. Thibault, T. Beetz, V. Elser, M. Howells, C. Jacobsen, J. Kirz, E. Lima, H. Miao, A. M. Neiman, and D. Sayre, Proc. Natl. Acad. Sci. USA **102**, 15343 (2005).
27. A. Schropp, R. Hoppe, V. Meier, J. Patommel, F. Seiboth, Y. Ping, D. G. Hicks, M. A. Beckwith, G. W. Collins, A. Higginbotham, J. S. Wark, H. J. Lee, B. Nagler, E. C. Galtier, B. Arnold, U. Zastrau, J. B. Hastings, and C. G. Schroer, Sci. Rep. **5**, 11089 (2015).